




# Preparation of $\text{Ti}^{3+}$ self-doped $\text{TiO}_x\text{NRs/rGO}$ composite: application in supercapacitors

Juan Ding<sup>1,\*</sup>  and Ligang Cheng<sup>2</sup>

<sup>1</sup>School of Textile, Zhongyuan University of Technology, Zhengzhou 451191, People's Republic of China

<sup>2</sup>School of Material Science & Engineering, Henan University of Technology, Zhengzhou 450001, People's Republic of China

Received: 28 April 2021

Accepted: 26 June 2021

Published online:

3 July 2021

© The Author(s), under exclusive licence to Springer Science+Business Media, LLC, part of Springer Nature 2021

## ABSTRACT

The characteristics of large surface area, high conductivity and mechanical flexibility performances make graphene suitable for high power next-generation energy storage devices. However, it only stores charge through double-layer capacitors, which limits its energy storage mechanism, resulting in a limited specific capacitance of graphene. In this paper, black  $\text{Ti}^{3+}$  self-doped nano titanium dioxide rods ( $\text{TiO}_x\text{NRs}$ ) were introduced into graphene nanosheets to improve capacitor performance. The results manifest that when 20 wt%  $\text{TiO}_x\text{NRs}$  were added into the  $\text{TiO}_x\text{NRs/rGO}$  composite, the capacitance performance is the best and the specific capacitance value is  $149.5 \text{ F g}^{-1}$  at the scanning speed of  $40 \text{ mV s}^{-1}$ . In addition, the specific capacitance of the electrode prepared with the  $\text{TiO}_x\text{NRs/rGO}$  composite still maintains the original 89.57% after 2000 charge–discharge cycles and has a good cycle life at a current density of  $1 \text{ A g}^{-1}$ . In short, the  $\text{TiO}_x\text{NRs/rGO}$  composite is a prospect and potential material for supercapacitor electrodes in the future.

## 1 Introduction

Supercapacitors, also known as electrochemical capacitors, are energy storage devices between traditional capacitors and traditional batteries. It is a good auxiliary power source and can be well applied in many power plants due to its advantages, such as long life, low cycle cost, good reversibility, fast charge and discharge, small internal resistance, high cycle efficiency and large output power [1–5].

Graphene is the thinnest material and has extraordinary characteristics due to its unique structure [6–8]. The excellent performances include good

electrical conductivity, high mechanical strength, good light transmittance, good thermal conductivity and thermal expansion coefficient, which have attracted special attention of researchers [9–14]. Therefore, graphene is widely used in fields such as physics, chemistry, biology, supercapacitors and microwave absorption materials [15–17]. In particular, the high conductivity and large specific surface area of graphene are appropriate as electrode materials for supercapacitors. However, due to the defects of the energy storage mechanism, the specific capacitance is limited [18–21].

Address correspondence to E-mail: dingjuan218485@126.com

Titanium oxide ( $\text{TiO}_2$ ) is a typical metal oxide.  $\text{TiO}_2$  has many excellent properties such as high natural abundance, stable electrochemical property, non-toxicity, low cost, good pseudocapacitance performance, high photocatalytic efficiency and good biocompatibility. Thus, it can be widely used in sensors, photocatalysis, dye-sensitized solar cells, biomedicine, lithium-ion batteries and supercapacitors, etc. [22–25]. Attentions on primary nano- $\text{TiO}_2$  structures of researchers are those of nanoparticles, one-dimensional  $\text{TiO}_2$  and  $\text{TiO}_2$  thin films. Among them, one-dimensional structure  $\text{TiO}_2$  has been concerned and extensively studied by researchers attributing to its larger specific surface area, structure particularity and charge transfer efficiency, etc. [26–29]. As is known, one-dimensional structure of nano- $\text{TiO}_2$  mainly includes nanorods, nanotubes, nanobelts, nanowires. He [30] et al. synthesized  $\text{TiO}_2$ NRs with electrospinning technology, and then heated in KOH solution for 1 h to finally obtain KOH-treated  $\text{TiO}_2$ -NRs. The results showed that  $\text{TiO}_2$ NRs can be used to prepare flexible supercapacitor electrodes, with a specific capacitance of  $65.84 \text{ F g}^{-1}$  at a scan rate of  $1 \text{ mV s}^{-1}$ . Selvakumar et al. [31] prepared activated carbon nanocomposite electrodes and  $\text{TiO}_2$  nanoparticles by a microwave method. The results manifested that the specific capacitance of the p/p symmetric supercapacitor is  $122 \text{ F g}^{-1}$ . Meanwhile, at current densities of  $2 \text{ mA cm}^{-2}$ ,  $4 \text{ mA cm}^{-2}$ ,  $6 \text{ mA cm}^{-2}$ , and  $7 \text{ mA cm}^{-2}$ , the specific capacitance of the supercapacitor stabilized at 5000 cycles. Lu [23] et al. reported that anodized  $\text{TiO}_2$  was calcined in hydrogen to obtain hydrogenated  $\text{TiO}_2$  ( $\text{H-TiO}_2$ ) with a scanning rate of  $100 \text{ mV s}^{-1}$ . The maximum specific capacity of  $\text{H-TiO}_2$  prepared at  $400 \text{ }^\circ\text{C}$  was  $3.24 \text{ mF cm}^{-2}$ , which is 40 times that of an air-annealed  $\text{TiO}_2$  capacitors under the same conditions. The initial specific capacitance is only 3.1% reduction after 10,000 cycles absolutely ascribed to its good long-term cycle stability.

In this study, in view of the disadvantages of graphene nanosheets that easy to agglomerate in the charging and discharging process of supercapacitors, black  $\text{Ti}^{3+}$  self-doped  $\text{TiO}_2$  nanoparticles were introduced into graphene nanosheets to solve the above problems. So as to achieve the purpose of enhancing the specific surface area and the capacitance performance.

## 2 Experimental section

### 2.1 Preparation of $\text{TiO}_x$ nanoparticles

10 M NaOH solution was slowly poured into the mixture of butyl titanate and isopropanol (volume ratio 1:2), reacted for 0.5 h under magnetic stirring. Then the mixed solution was reacted in a 100 mL polytetrafluoroethylene hydrothermal kettle at  $180 \text{ }^\circ\text{C}$  for 20 h. Natural cooling to room temperature, washed the precipitate with deionized water several times and then washed with 0.1 M HCl solution until the pH value was close to 7. Then, replaced the sodium ions with hydrochloric acid of the above concentration for 10 h. Finally, washed with deionized water until the pH value was close to 7, filtered and dried at  $80 \text{ }^\circ\text{C}$  for 24 h [32].

The above product was thoroughly mixed with  $\text{NaBH}_4$  with a mass fraction of 1:2 and ground at room temperature for 30 min. Then, the mixture was transferred to a porcelain boat and placed in a tubular furnace for 2 h at a heating rate of  $5 \text{ }^\circ\text{C/min}$  from room temperature to  $350 \text{ }^\circ\text{C}$  in an Air environment. After natural cooling to room temperature,  $\text{TiO}_x$  nanorods were obtained, washed with deionized water and anhydrous ethanol several times, dried at  $80 \text{ }^\circ\text{C}$  for 24 h. In the absence of  $\text{NaBH}_4$ ,  $\text{TiO}_2$  nanorods were synthesized under the same condition for comparison [33–35].

### 2.2 Preparation of $\text{TiO}_x/\text{rGO}$ composite

Firstly, graphene oxide (GO) was synthesized by a modified Hummers' method [36]. A certain amount of prepared GO was dispersed in deionized water to form a  $4 \text{ mg/mL}$  suspension. Then a certain mass of  $\text{TiO}_x$  was added in proportion with ultrasonic treatment for 30 min. After that,  $\text{TiO}_x/\text{GO}$  composite was poured into a three-point flask, and then certain amount of hydrazine hydrate (the ratio of  $\text{TiO}_x/\text{GO}$  composite to hydrazine hydrate was 1:10) was added into the above mixture under reflux condensation at  $95 \text{ }^\circ\text{C}$  for 24 h. Finally, the obtained composite was washed with deionized water and absolute ethyl alcohol several times, dried at  $80 \text{ }^\circ\text{C}$  for 24 h. The preparation process of the  $\text{TiO}_x$ NRs/rGO composite is shown in Fig. 1.

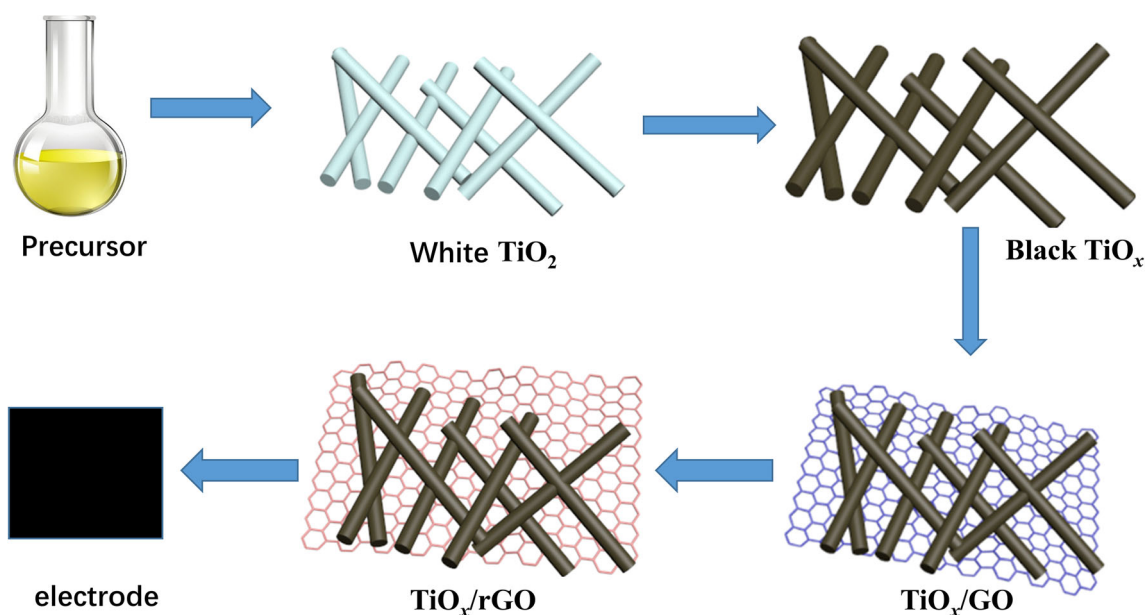


**Fig. 1** The preparation process of the  $\text{TiO}_x\text{NRs/rGO}$  composite

### 2.3 Preparation and electrochemical measurement of working electrode

A three-electrode system was selected as the electrochemical test. The preparation of working electrode was as follows: Polyvinylidene fluoride (PVDF) powder and acetylene black were chosen as the binder and conductive agent, respectively. The  $\text{TiO}_x\text{NRs/rGO}$  composite was mixed with PVDF and acetylene black in a mass ratio of 8:2:1, appropriate amount of NMP solution was added into the above mixture and stirred to make the mixture into a slurry. After that, the slurry was placed in an agate mortar and grind it clockwise to a mushy. The polished paste was coated into the positive and negative electrode areas with an area of  $1\text{ cm} \times 1\text{ cm}$  at one end of a nickel foam, which was pretreated with 3 M HCl with an area of  $1\text{ cm} \times 2\text{ cm}$ , dried at  $80\text{ }^\circ\text{C}$  for 24 h. Finally, the foam was pressed into a sheet under a pressure of 8 MPa to obtain a working electrode.

### 2.4 Characterization

FTIR spectrometer (FTIR 650, Shimadzu, Japan) was used to analyze the structure of the samples. The crystal structure of the sample was determined by X-ray diffraction (XRD, Philips X' Pert, Holland) and X-ray Photoelectron Spectroscopy (XPS, Thermo Scientific ESCALAB 250, USA) was applied to analyze the elements on the surface of the composite. The main parameters of rGO were represented by Raman

spectrometer (Lab RAM HR, HJY, France). The morphology of the sample was observed by Field Emission Scanning Electron Microscopy (FESEM, FEI Sirion-200, USA). The electrochemistry workstation for laboratory (RST 5000, SHIRUISI Instrument, Zhengzhou, China) can be used to test conduct cyclic voltammetry, charge and discharge and electrochemical impedance in electrode materials. A three-electrode system was selected to test, with 4 M KOH solution as the electrolyte. The saturated calomel electrode was used as the reference electrode, and the platinum wire was used as the counter electrode. The test voltage ranges of CV and GCD is  $-0.1$  to  $0.4\text{ V}$ , the current density of GCD test is  $1\text{ A/g}$ , and the frequency of EIS test is  $10\text{ MHz} \sim 100\text{ kHz}$  and the amplitude is  $7\text{ mV}$ . Before testing, the electrode was soaked for 30 min for electrochemical test.

## 3 Results and discussion

### 3.1 FTIR analysis

The FTIR spectrum of the  $\text{TiO}_x\text{NRs/rGO}$  composite is observed in Fig. 2. The broad peak appears at  $3174\text{ cm}^{-1}$  attributing to the O–H stretching vibration of the hydroxyl group. It is noteworthy that there is a wide peak of the  $\text{TiO}_x\text{NRs/rGO}$  composite near  $1633\text{ cm}^{-1}$ , which is considered to be the characteristic peak of the in-plane vibration of graphene nanosheets. The peak near  $913\text{ cm}^{-1}$  is mainly due to

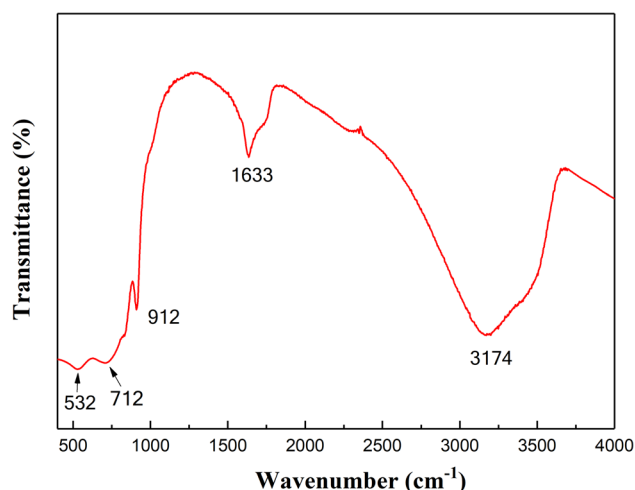


**Fig. 2** The FTIR spectrum of the  $\text{TiO}_x\text{NRs/rGO}$  composite

the bending vibration absorption peak of the C–H bond on the benzene ring. There are two small peaks below  $900\text{ cm}^{-1}$ , which are consistent with the tensile vibration peak of the Ti–O–Ti bond.

### 3.2 XRD analysis

It can be seen from Fig. 3 that rGO has a broad peak at  $25.48^\circ$ , corresponding to the characteristic peak of rGO, which indicates that GO is largely reduced to rGO. As shown in Fig. 3,  $\text{TiO}_x\text{NRs}$  and  $\text{TiO}_x\text{NRs/rGO}$  composites have basically the same diffraction peaks at  $25.3^\circ$ ,  $37.8^\circ$ ,  $48.1^\circ$ ,  $53.9^\circ$  and  $55.1^\circ$ . These peaks can be judged by the XRD standard pattern (ICSD No. 01-086-1156). In addition, the XRD curve of  $\text{TiO}_x$  contains TiO crystal form (ICSD No. 01-073-9742) and  $\text{TiO}_{1.25}$  (ICSD No. 01-078-5811) crystal

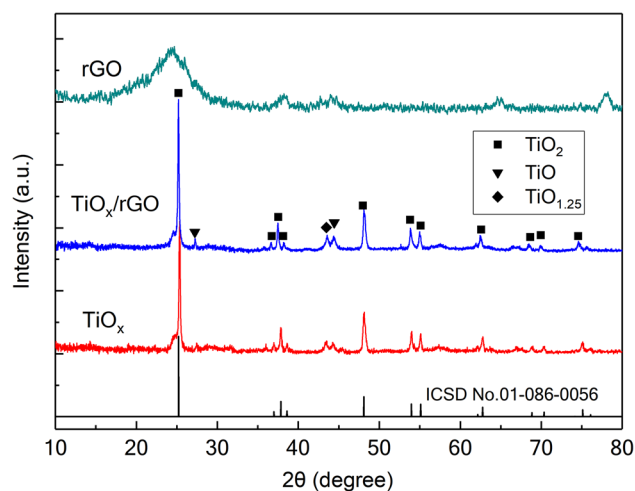


**Fig. 3** XRD patterns of rGO,  $\text{TiO}_x\text{NRs}$  and  $\text{TiO}_x\text{NRs/rGO}$

form, which is a manifestation of  $\text{TiO}_2$  being reduced. Only the diffraction peak of  $\text{TiO}_x$  exists in the  $\text{TiO}_x\text{NRs/rGO}$  composite, and the broad peak of rGO disappears. This is because the diffraction peaks of  $\text{TiO}_x$  nanorods and rGO both appear at about  $25^\circ$ ; however, the peak intensity of the  $\text{TiO}_x$  nanorods is so high that the broad weak peak of rGO cannot be observed.

### 3.3 Raman spectrum analysis

Figure 4 shows the Raman spectra of rGO and  $\text{TiO}_x/\text{rGO}$  composite, which contains 20%  $\text{TiO}_x$  nanorods. A series peaks ( $112\text{ cm}^{-1}$ ,  $363\text{ cm}^{-1}$ ,  $492\text{ cm}^{-1}$ ,  $619\text{ cm}^{-1}$ ) less than  $1000\text{ cm}^{-1}$  in the  $\text{TiO}_x/\text{rGO}$  composite are Raman characteristic peaks of  $\text{TiO}_x$ . The two peaks appearing at  $1349\text{ cm}^{-1}$  and  $1585\text{ cm}^{-1}$  are D peak reflecting the structural defects of graphene and the G peak indicating the in-plane vibration of the  $\text{sp}^2$  carbon atom, respectively. The ratio of peak intensity ( $I_D: I_G$ ) less than 1 manifests that GO is reduced to rGO throughly [37]. In summary, the  $\text{TiO}_x/\text{rGO}$  composite is composed of  $\text{TiO}_x$  nanorods and rGO, the result of which is consistent with the XRD pattern.

### 3.4 XPS spectra analysis

Figure 5 displays the XPS spectra of the  $\text{TiO}_x/\text{rGO}$  composite. In Fig. 5a, the C 1s, Ti 2p and O 1s are observed in the XPS wide scan spectra of the  $\text{TiO}_x/\text{rGO}$  composite. There are no other impurity peaks observed in the spectrum proving that the composite is pure. The C 1s spectrum of the  $\text{TiO}_x/\text{rGO}$

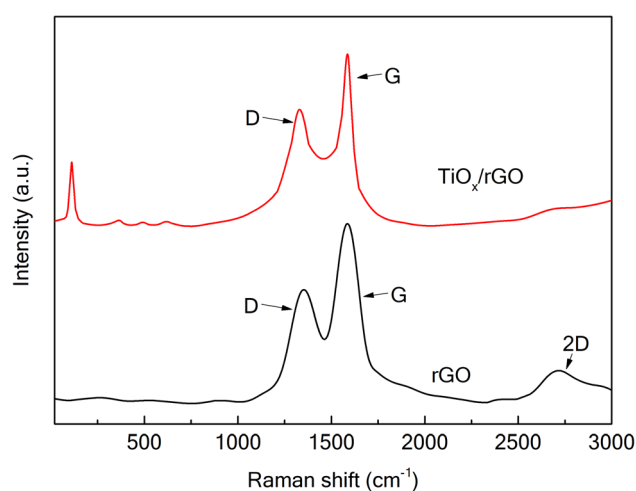


**Fig. 4** Raman spectrum of rGO and  $\text{TiO}_x/\text{rGO}$

composite are revealed in Fig. 5b, the binding energy of C–C, C=C and C–H bonds appears at 284.6 eV. The chemical shift to greater binding energy results in the peaks at 285.7 eV, 287.5 eV and 289.2 eV, corresponding to the C–OH bond, C=O bond and O=C–OH bond, respectively. Figure 5c, d manifest the XPS spectrum of the Ti 2p orbital. Figure 5c displays the XPS spectrum of  $\text{TiO}_2$ , there are two strong signal peaks at 458.6 eV and 464.5 eV, corresponding to Ti 2p 3/2 and Ti 2p 1/2 of  $\text{Ti}^{4+}$ , respectively. There are two main signal peaks of  $\text{TiO}_x$  at 458.6 eV and 463.5 eV can be clearly observed in Fig. 5d. They are derived from Ti 2p 3/2 and Ti 2p 1/2 of  $\text{Ti}^{4+}$ , respectively. While two weak acromial peaks at 456.4 eV and 461.8 eV correspond to Ti 2p 3/2 and Ti 2p 1/2 of  $\text{Ti}^{3+}$ , respectively, indicating the existence of  $\text{Ti}^{3+}$  in  $\text{TiO}_x$  /rGO composite.

### 3.5 FESEM analysis

As shown in Fig. 6a, the average diameter and length of  $\text{TiO}_x$  nanorods with smooth surface are about 50 nm and 1.5  $\mu\text{m}$ , respectively. It can be seen in Fig. 6b that the rGO nanosheets are transparent and undulated like waves, indicating that the nanosheets are thin. This is because some folds are still retained after GO was reduced to rGO. In Fig. 6c, d,  $\text{TiO}_x$  nanorods are evenly distributed in rGO nanosheets, and some  $\text{TiO}_x$ NRs and rGO are interwoven together to form a network structure, which can reduce the agglomeration of rGO nanosheets.

### 3.6 Electrical performance analysis

The charge–discharge curves of  $\text{TiO}_x$ /rGO composite with different mass fractions of  $\text{TiO}_x$  (0 wt%, 10 wt%,

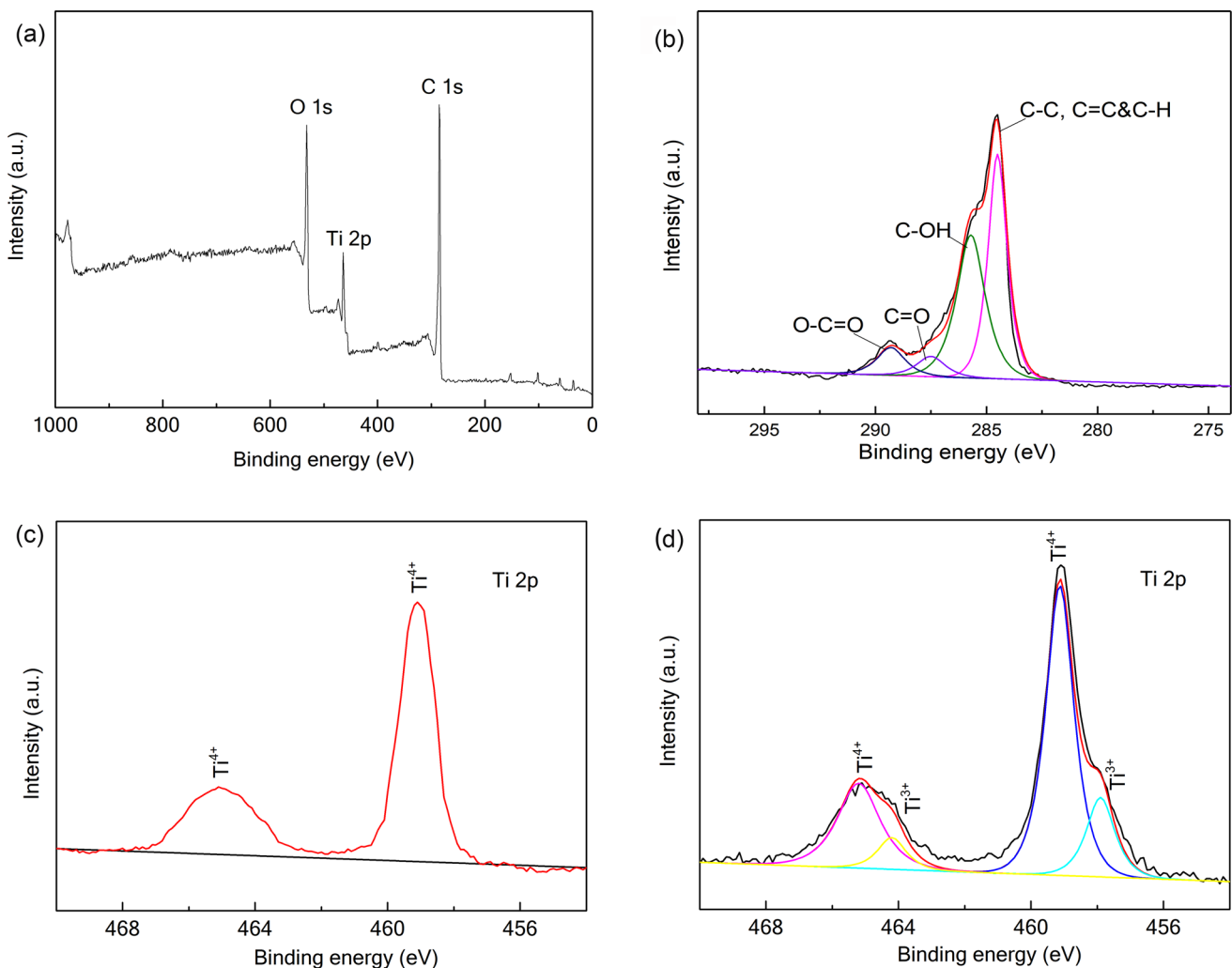


**Fig. 5** The XPS wide scan spectra (a), elements C 1s (b),  $\text{TiO}_2$  (c) and  $\text{TiO}_x$  (d) of the  $\text{TiO}_x$ /rGO composite

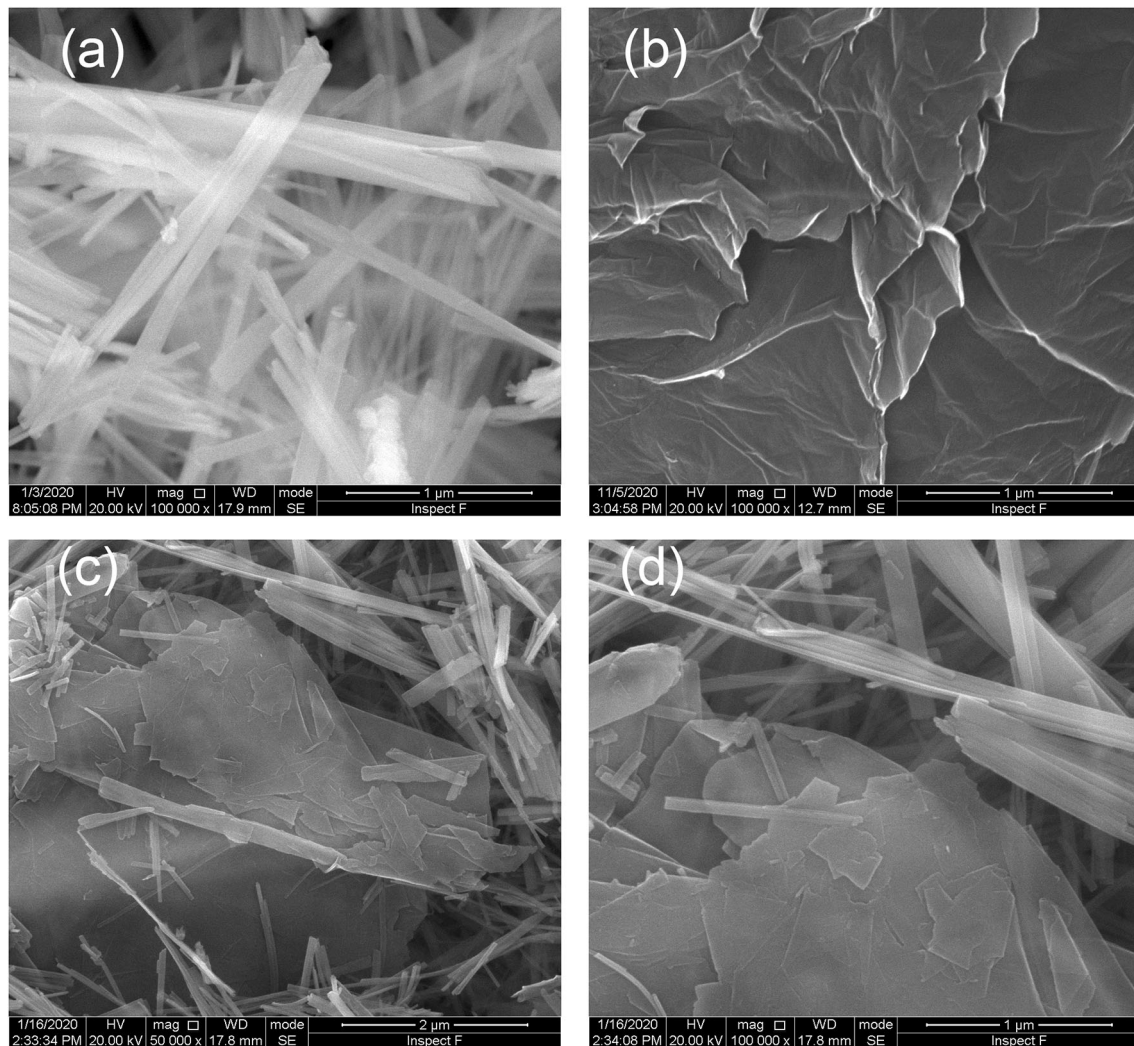


**Fig. 6** FESEM images of TiO<sub>x</sub> nanorods (a), FESEM images of rGO (b), FESEM images of TiO<sub>x</sub>/rGO (c and d)

20 wt%, 30 wt% and 40 wt%) at a constant current of  $1 \text{ A g}^{-1}$  is displayed in Fig. 7a. The charging curve corresponds to the positive scan curve in the cyclic voltammetry curve while the discharge curve is consistent with the negative scan curve in the cyclic voltammetry curve. The two platforms represented the oxidation peak and reduction peak independently. As shown in Fig. 7a, the charge and discharge potential of TiO<sub>x</sub>/rGO composite changes non-linearly with time, indicating that the Faraday reaction exists in the charge storage process. In addition, the longest charge–discharge time is the TiO<sub>x</sub>/rGO composite with 20 wt% TiO<sub>x</sub> nanorods at the same charge–discharge current density, which makes clear that more charge can be stored in the TiO<sub>x</sub>/rGO composite with 20 wt% TiO<sub>x</sub> nanorods comparing to other TiO<sub>x</sub> content of the composite. It can be seen

from Fig. 7b that as the current density increases, the specific capacitance decreases. This is because as the current density increases, the charge–discharge rate increases and the electrode reaction is insufficient. When the current density is  $1 \text{ A/g}$  and  $10 \text{ A/g}$ , the specific capacitance of the composite material is  $149.5 \text{ F/g}$  and  $89.2 \text{ F/g}$ , respectively, which shows that the composite material has excellent rate performance.

In order to measure the electrochemical properties of the TiO<sub>x</sub>/rGO composite, CV test is performed according to the electrochemical workstation in the laboratory. The specific capacitance of the TiO<sub>x</sub>/rGO composite can be calculated according to the CV curves. The calculation formula is as follows:

$$C_s = \left( \int IdV \right) / vm\Delta V \quad (1)$$

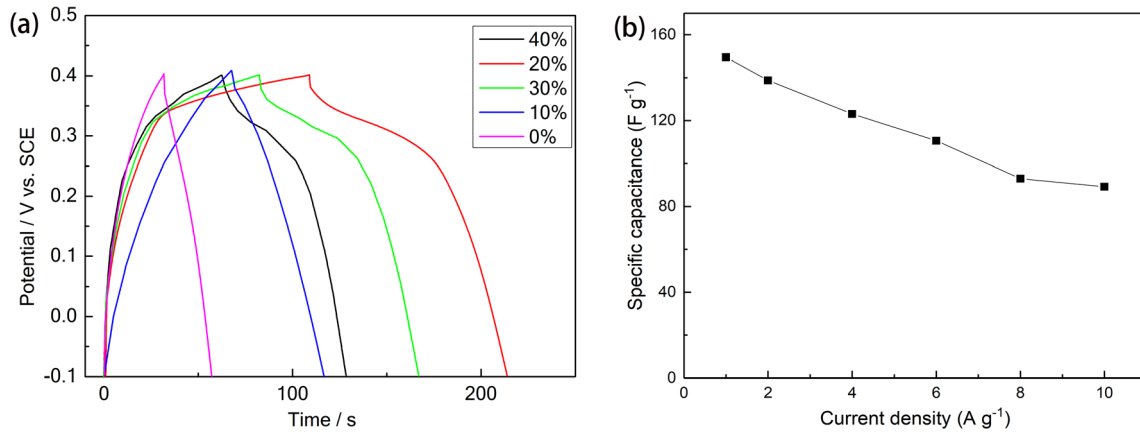


**Fig. 7** **a** Constant current charge–discharge curves of  $\text{TiO}_x/\text{rGO}$  composite with different mass fractions of  $\text{TiO}_x$  (0 wt%, 10 wt%, 20 wt%, 30 wt% and 40 wt%) nanorods at  $1 \text{ A g}^{-1}$ . **b** is the specific capacitance of  $\text{TiO}_x/\text{rGO}$  composite ( $\text{TiO}_x$  20 wt%) at different current densities

where  $C_s$  represents specific capacitance;  $I$  is the current;  $V$  displays the scanning rate;  $M$  expresses the weight of active substance;  $\Delta V$  signifies the potential window. According to Eq. (1), at the same scanning rate, the larger the area enclosed by CV curve is, the larger the specific capacitance is.

Figure 8a manifests the cyclic voltammograms of the  $\text{TiO}_x/\text{rGO}$  composite at different scan rates, in which there is a pair of obvious Faraday redox peaks, indicating that the  $\text{TiO}_x/\text{rGO}$  composite acts as a pseudo capacitance. Under the action of diffusion control and polarization, the Faraday redox peak moves to the direction of a more positive potential and a more negative potential with the increase of scan rate [38, 39]. When the scan rate was increased from 10 to  $80 \text{ mV s}^{-1}$ , the oxidation peak and reduction peak shifted by 70 mV and 20 mV, respectively. The specific capacitance is  $117.3 \text{ F g}^{-1}$ ,

$125.2 \text{ F g}^{-1}$ ,  $149.5 \text{ F g}^{-1}$  and  $122.4 \text{ F g}^{-1}$ , corresponding to the scan rate at  $10 \text{ mV s}^{-1}$ ,  $20 \text{ mV s}^{-1}$ ,  $40 \text{ mV s}^{-1}$  and  $80 \text{ mV s}^{-1}$ , respectively. Figure 8b lists the comparison of cyclic voltammetry of  $\text{TiO}_x/\text{rGO}$ ,  $\text{TiO}_2/\text{rGO}$  and  $\text{rGO}$  composites with a scan rate at  $40 \text{ mV s}^{-1}$ . As can be seen in Fig. 8 that the curve area of the  $\text{TiO}_x/\text{rGO}$  composite is larger than that of  $\text{TiO}_2/\text{rGO}$  composite and  $\text{rGO}$ , revealing the capacity of charge storage of the  $\text{TiO}_x/\text{rGO}$  composite is greater. The reasons are as follows: First,  $\text{TiO}_x/\text{rGO}$  includes both the double-layer capacitance produced by graphene and the pseudo capacitance produced by  $\text{TiO}_x$ . The combination of the two materials improves the overall energy storage capacity. Secondly, the presence of  $\text{TiO}_x$  nanorods is beneficial to reduce the agglomeration of graphene and increase the contact area between the material and the electrolyte, thereby improving the performance of the composite. By calculating the specific capacitances of

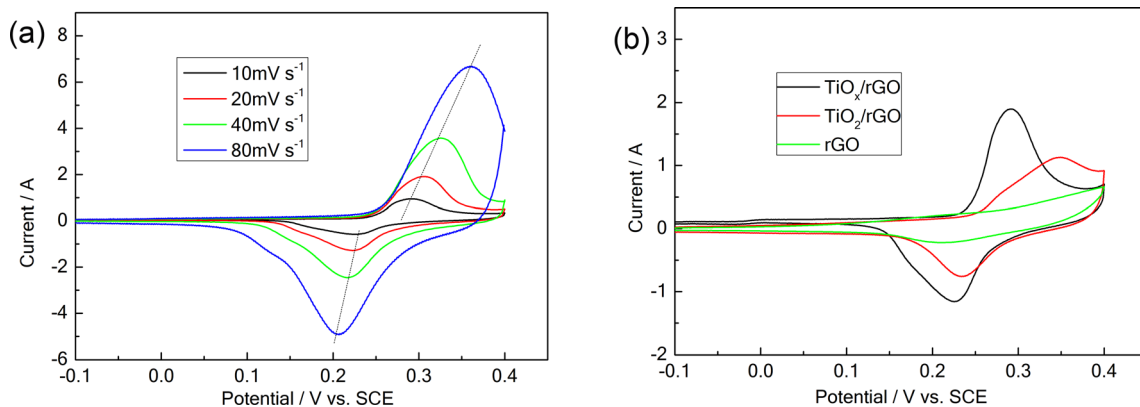


**Fig. 8** **a** CV curves of  $\text{TiO}_x/\text{rGO}$  composite at different scanning rates. **b** CV curves of  $\text{TiO}_x/\text{rGO}$  composite,  $\text{TiO}_2/\text{rGO}$  and  $\text{rGO}$  at  $10 \text{ mV s}^{-1}$

TiO<sub>x</sub>/rGO, TiO<sub>2</sub>/rGO and rGO composites are 149.5 F g<sup>-1</sup>, 118.6 F g<sup>-1</sup> and 76.4 F g<sup>-1</sup>, respectively at the scan rate 40 mV s<sup>-1</sup>. Thus, the TiO<sub>x</sub> nanorods reduction by TiO<sub>2</sub> nanorods improve the capacitance performance of the TiO<sub>x</sub>/rGO composite.

Cyclic performance is an important index to characterize the sustainable use of materials. The change of capacity can be investigated by constant current charge–discharge test. Based on the above reasons, the stability of the TiO<sub>x</sub>/rGO composite was tested at a current density of 1 A g<sup>-1</sup>. As shown in Fig. 9, the capacitance retention rate still reaches 89.57% after 2 000 cycles, indicating that the TiO<sub>x</sub>/rGO composite has excellent cycle stability.

Typical impedance behavior of supercapacitors is analyzed by Nyquist graph. Figure 10 describes the dependence of real part  $Z'$  and imaginary part  $Z''$  impedance in the frequency range of 10 MHz ~ 100 kHz. In Fig. 10a, the observed regions are high frequency and medium frequency impedance regions, which basically represent the electrolyte internal resistance characteristics  $R_S$  and the interface charge transfer resistance  $R_{CT}$  of the supercapacitor system. A semicircle fitted from the impedance data of the Nyquist diagrams in the high and medium frequency regions is the result of the parallel interaction between the charge transfer resistance and the double-layer capacitor ( $C_{dl}$ ) at the electrode–electrolyte interface, as shown in the equivalent circuit in Fig. 10. Therefore, the internal resistance  $R_S$  ( $R_S = 0.9 \Omega$ ) can be calculated by the real part  $Z'$  intercept after the circuit is closed. The IF intercept of the semicircle produces  $R_S + R_{CT}$ , resulting in  $R_{CT}$  ( $R_{CT} = 3.5 \Omega$ ),

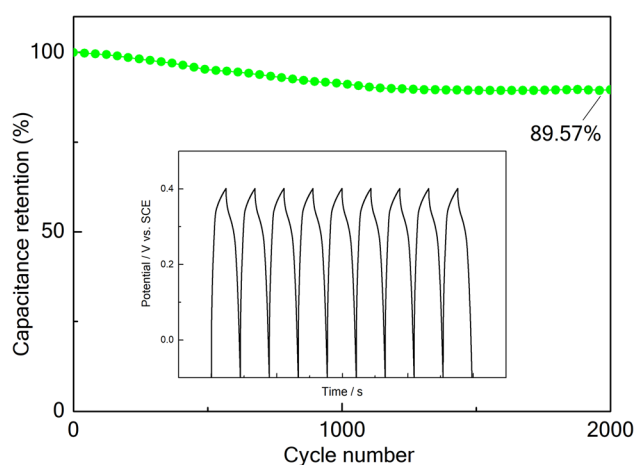


**Fig. 9** Charge–discharge profile of the TiO<sub>x</sub>/rGO composite at a current density of 1 A g<sup>-1</sup>

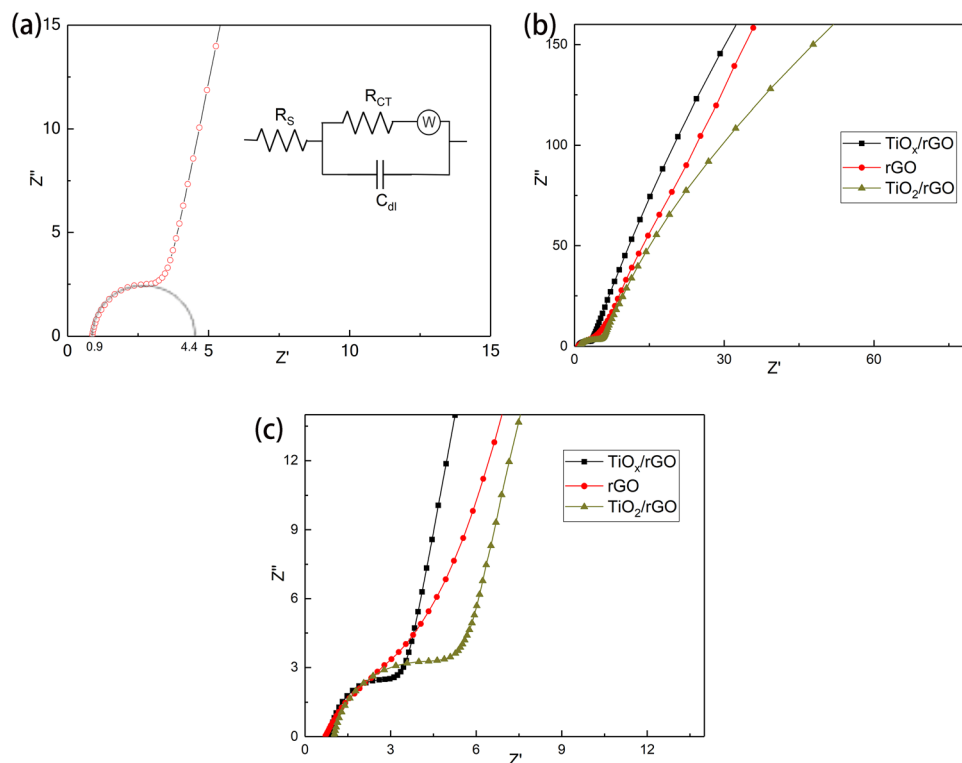
which is a relatively low resistance value. Besides, the higher the slope of the line in the low and middle frequency region, the smaller the resistance, which reveals the diffusion resistance of electrolyte ions at the electrode gap. The straight slope, in the right low frequency part of the Nyquist curve of the TiO<sub>x</sub>NRs/rGO composite electrode, is large. The result indicates that the diffusion rate of electrolyte ions in the TiO<sub>x</sub>NRs/rGO composite electrode is high. Figure 10b and c are comparison diagrams of the EIS diagrams of TiO<sub>2</sub>/rGO, rGO and TiO<sub>x</sub>NRs/rGO composites. From this, the impedance semicircle of TiO<sub>x</sub>/rGO composite is significantly smaller than that of TiO<sub>2</sub>/rGO and the slope of TiO<sub>x</sub>/rGO is greater than that of TiO<sub>2</sub>/rGO in the low frequency area, which shows that the TiO<sub>x</sub>NRs/rGO composite has better capacitance characteristics. In addition, there is almost no semicircle in rGO in the figure, indicating that the charge transfer resistance is low, impedance is low, and conductivity is good.

## 4 Conclusion

In summary, the TiO<sub>x</sub>NRs/rGO composite was prepared with a three-step method. Firstly, TiO<sub>2</sub> nanorods were synthesized with a one-step hydrothermal method under alkaline condition. Then, TiO<sub>2</sub> nanorods were reduced into TiO<sub>x</sub> nanorods through solid phase reduction. Finally, TiO<sub>x</sub>NRs/rGO composite was prepared in liquid phase. rGO nanosheets are relatively thin. The average diameter and length of the TiO<sub>x</sub>/NRs composite is about 50 nm and 1.5 μm, respectively, which are evenly dispersed among rGO nanosheets. In addition, the mass ratio effect of TiO<sub>x</sub>NRs and rGO on the capacitance performance of TiO<sub>x</sub>NRs/rGO composite is studied. The results show that the specific capacitance of TiO<sub>x</sub>NRs/rGO composite is improved compared with that of TiO<sub>2</sub>/rGO composite and rGO nanosheets. When the mass ratio the TiO<sub>x</sub>NRs composite was 20 wt% in the TiO<sub>x</sub>/rGO composite, the specific capacitance of TiO<sub>x</sub>/rGO composite reaches the best (149.5 F g<sup>-1</sup>) at the scan rates of 40 mV s<sup>-1</sup>. In addition, at the current density of 1 A g<sup>-1</sup>, the specific capacitance of TiO<sub>x</sub>NRs/rGO composite remains 89.57% after 2000 cycles. Therefore, as the electrode of supercapacitor, the TiO<sub>x</sub>NRs/rGO composite exhibits excellent cycling stability and good electrochemical



**Fig. 10** **a** EIS diagram of  $\text{TiO}_x/\text{rGO}$  composite, **b** and **c** are the comparison diagrams of the EIS diagrams of  $\text{TiO}_2/\text{rGO}$ , rGO and  $\text{TiO}_x\text{NRs}/\text{rGO}$  composite materials



performances. In a word, it is a kind of material with great potential and application prospect in the future.

### Author contributions

All authors contributed to the study conception and design. Material preparation, data collection and analysis were performed by JD and LC. The first draft of the manuscript was written by JD and all authors commented on previous versions of the manuscript. All authors read and approved the final manuscript.

### Funding

The authors acknowledge the financial support from the Henan Province Science and Technology Project (Grant No. 212102210584), Cultivation Project of “Young Key Teachers in Universities of Henan Province, Funded by Young Key Teachers of Zhongyuan Institute of Technology” in 2019 (Jiaogao [2019] No. 350, Zhong Gonggong [2018] No. 60).

### Data availability

Written informed consent for publication of this paper was obtained from the Zhongyuan University of Technology and all authors.

### Declarations

**Conflict of interest** The authors declare that they have no conflict and competing of interest.

### References

1. N.L. Wu, Nanocrystalline oxide supercapacitors. *Mater. Chem. Phys.* **75**(1–3), 6–11 (2002)
2. G. Zhang, T. Wang, X. Yu, H. Zhang, H. Duan, B. Lu, Nanoforest of hierarchical  $\text{Co}_3\text{O}_4@\text{NiCo}_2\text{O}_4$  nanowire arrays for high-performance supercapacitors. *Nano Energy* **2**(5), 586–594 (2013)
3. R. Wei, Y. Gu, L. Zou, B. Xi, Q. Xu, Nanoribbon superstructures of graphene nanocages for efficient electrocatalytic hydrogen evolution. *Nano Lett.* **20**(10), 7342–7349 (2020)
4. W. Hailiang, L. Yongye, D. Hongjie, S.C. Hernan,  $\text{Ni}(\text{OH})_2$  nanoplates grown on graphene as advanced electrochemical pseudocapacitor materials. *J. Am. Chem. Soc.* **132**(21), 7472–7477 (2010)

5. L. Wang, B. Wen, X. Bai, C. Liu, H. Yang, NiCo Alloy/carbon nanorods decorated with carbon nanotubes for microwave absorption. *ACS Appl. Nano Mater.* **2**(12), 7827–7838 (2019)
6. X. Zhang, X. Xu, Y. Hu, G. Xu, W. He, J. Zhu,  $C_{60}/Na_4FeO_3/Li_3V_2(PO_4)_3$ /soft carbon quaternary hybrid superstructure for high-performance battery-supercapacitor hybrid devices. *NPG Asia Mater.* **12**(1), 8 (2020)
7. X. Yi, W. He, X. Zhang, Y. Yue, G. Yang, Z. Wang, M. Zhou, L. Wang, Graphene-like carbon sheet/Fe<sub>3</sub>O<sub>4</sub> nanocomposites derived from soda papermaking black liquor for high performance lithium ion batteries. *Electrochim. Acta* **232**, 550–560 (2017)
8. X. Yi, Y. Zhang, W. He, X. Zhang, G. Yang, Z. Wang, Y. Wang, Q. Cheng, Low-temperature synthesis of graphene/SiC nanocomposite anodes with super-long cycling stability. *ChemElectroChem* **4**(6), 1320–1326 (2017)
9. Y. Wang, X. Gao, X. Wu, W. Zhang, Q. Wang, C. Luo, Hierarchical ZnFe<sub>2</sub>O<sub>4</sub>@RGO@CuS composite: Strong absorption and wide-frequency absorption properties. *Ceram. Int.* **44**(8), 9816–9822 (2018)
10. L. Liu, L. Wang, Q. Li, X. Yu, X. Shi, J. Ding, W. You, L. Yang, Y. Zhang, R. Che, High-performance microwave absorption of MOF-derived core-shell Co@N-doped carbon anchored on reduced graphene oxide. *ChemNanoMat* **5**(4), 558–565 (2019)
11. I. Abdalla, A. Elhassan, J. Yu, Z. Li, B. Ding, A hybrid comprised of porous carbon nanofibers and rGO for efficient electromagnetic wave absorption. *Carbon* **157**, 703–713 (2020)
12. S. Wang, Y. Xu, R. Fu, H. Zhu, Y. Zhao, Rational construction of hierarchically porous Fe–Co/N-doped carbon/rGO composites for broadband microwave absorption. *Nano-Micro Lett.* **11**(4), 1–16 (2019)
13. B. Hu, C. Guo, C. Xu, Y. Cen, J. Hu, Y. Li, S. Yang, Y. Liu, D. Yu, C. Chen, Rational construction of V<sub>2</sub>O<sub>5</sub>@rGO with enhanced pseudocapacitive storage for high-performance flexible energy storage device. *ChemElectroChem* **6**(23), 5845–5855 (2019)
14. Y. Wang, X. Gao, W. Zhang, C. Luo, L. Zhang, P. Xue, Synthesis of hierarchical CuS/RGO/PANI/Fe<sub>3</sub>O<sub>4</sub> quaternary composite and enhanced microwave absorption performance. *J. Alloy. Compd.* **757**, 372–381 (2018)
15. H. Zhang, C. Lu, C. Chen, L. Xie, P. Zhou, Q. Kong, 2D layered  $\alpha$ -Fe<sub>2</sub>O<sub>3</sub>/rGO flexible electrode prepared through colloidal electrostatic self-assembly. *ChemElectroChem* **4**(8), 1990–1996 (2017)
16. Q. Zeng, X. Xiong, P. Chen, Q. Yu, Q. Wang, R. Wang, H. Chu, Air@rGO/Fe<sub>3</sub>O<sub>4</sub> microspheres with spongy shells: self-assembly and microwave absorption performance. *J. Mater. Chem. C* **4**(44), 10518–10528 (2016)
17. J.S. Sanchez, A. Pendashteh, J. Palma, M. Anderson, R. Marcilla, Anchored Fe<sub>3</sub>O<sub>4</sub> nanoparticles on rGO nanosheets as high-power negative electrodes for aqueous batteries. *ChemElectroChem* **4**(6), 1295–1305 (2017)
18. L. Liu, J. Lang, P. Zhang, B. Hu, X. Yan, Facile synthesis of Fe<sub>2</sub>O<sub>3</sub> nano-dots@nitrogen-doped graphene for supercapacitor electrode with ultralong cycle life in KOH electrolyte. *ACS Appl. Mater. Interfaces* **8**(14), 9335–9344 (2016)
19. M.D. Stoller, S. Park, Y. Zhu, J. An, R.S. Ruoff, Graphene-based ultracapacitors. *Nano Lett.* **8**(10), 3498–3502 (2008)
20. Z. Xu, Z. Zhang, H. Yin, S. Hou, H. Lin, J. Zhou, S. Zhuo, Investigation on the role of different conductive polymers in supercapacitors based on a zinc sulfide/reduced graphene oxide/conductive polymer ternary composite electrode. *RSC Adv.* **10**(6), 3122–3129 (2020)
21. Y. Li, M.V. Zijll, S. Chiang, P. Ning, KOH modified graphene nanosheets for supercapacitor electrodes. *J. Power Sources* **196**(14), 6003–6006 (2011)
22. D. Wang, X. Li, J. Chen, X. Tao, Enhanced photoelectrocatalytic activity of reduced graphene oxide/TiO<sub>2</sub> composite films for dye degradation. *Chem. Eng. J.* **198**, 547–554 (2012)
23. X. Lu, G. Wang, T. Zhai, M. Yu, Y. Li, Hydrogenated TiO<sub>2</sub> nanotube arrays for supercapacitors. *Nano Lett.* **12**(3), 1690–1696 (2012)
24. M.M. Abutalib, A. Rajeh, Influence of MWCNTs/Li-doped TiO<sub>2</sub> nanoparticles on the structural, thermal, electrical and mechanical properties of poly (ethylene oxide)/poly (methylmethacrylate) composite. *J. Organomet. Chem.* **918**, 121309 (2020)
25. M. Kazazi, Z.A. Zafar, M. Delshad, J. Cervenka, C. Chen, TiO<sub>2</sub>/CNT nanocomposite as an improved anode material for aqueous rechargeable aluminum batteries. *Solid State Ion.* **320**, 64–69 (2018)
26. S. Muthusamy, J. Charles, Metal–organic framework of nanostructured polypyrrole incorporated with TiO<sub>2</sub> nanoparticles for supercapacitor electrode. *J. Mater. Sci.* **32**(6), 7349–7365 (2021)
27. L.Y. Zhu, Zemin, Z. Zhou, M. Zhu, Preparation of TiO<sub>2</sub> nanowires-reduced graphene oxide composites by one-step hydrothermal method for supercapacitor. *Mod. Chem. Indust.* **39**, 146–150 (2019).
28. J. Macak, M. Zlamal, J. Krysa, P. Schmuki, Self-organized TiO<sub>2</sub> nanotube layers as highly efficient photocatalysts. *Small* **3**(2), 300–304 (2010)
29. J.M. Macak, S. Aldabergerova, A. Ghicov, P. Schmuki, Smooth anodic TiO<sub>2</sub> nanotubes: annealing and structure. *Phys. Status Solidi* **203**(10), R67–R69 (2010)

30. X. He, C.P. Yang, G.L. Zhang, D.W. Shi, Q.A. Huang, H.B. Xiao, Y. Liu, R. Xiong, Supercapacitor of TiO<sub>2</sub> nanofibers by electrospinning and KOH treatment. *Mater. Des.* **106**, 74–80 (2016)
31. M. Selvakumar, D.K. Bhat, Microwave synthesized nanostructured TiO<sub>2</sub>-activated carbon composite electrodes for supercapacitor. *Appl. Surf. Sci.* **263**, 236–241 (2012)
32. J. Ding, L. Cheng, X. Zhang, Q. Liu, Synthesis of multilayered micro flower NiCo<sub>2</sub>O<sub>4</sub>/GN/Fe<sub>3</sub>O<sub>4</sub> composite for enhanced electromagnetic microwave (EM) absorption performance. *J. Mater. Sci.* **30**(9), 8864–8875 (2019)
33. J. Liu, S. Shao, B. Meng, G. Fang, Z. Xie, L. Wang, X. Li, Enhancement of inverted polymer solar cells with solution-processed ZnO-TiO<sub>x</sub> composite as cathode buffer layer. *Appl. Phys. Lett.* **100**(21), 213906 (2012)
34. X. Bao, L. Sun, W. Shen, C. Yang, W. Chen, R. Yang, Facile preparation of TiO<sub>x</sub> film as an interface material for efficient inverted polymer solar cells. *J. Mater. Chem.* **2**(6), 1732–1737 (2014)
35. M. Nakamura, S. Kato, T. Aoki, L. Sirghi, Y. Hatanaka, Formation mechanism for TiO<sub>x</sub> thin film obtained by remote plasma enhanced chemical vapor deposition in H<sub>2</sub>-O<sub>2</sub> mixture gas plasma. *Thin Solid Films* **401**(1), 138–144 (2001)
36. L. Cheng, Q. Wang, J. Ding, One-step hydrothermal synthesis of the FeNi<sub>3</sub>/rGO composite for electrochemical supercapacitor. *J Mater Sci: Mater Electron* **32**(6), 7226–7236 (2021)
37. H. Yue, E. Guan, X. Gao, F. Yao, Q. Wang, T. Zhang, Z. Wang, S. Song, H. Zhang, One-step hydrothermal synthesis of TiO<sub>2</sub> nanowires-reduced graphene oxide nanocomposite for supercapacitor. *Ionics* **25**, 1–8 (2018)
38. L. Mei, T. Yang, C. Xu, M. Zhang, L. Chen, Q. Li, T. Wang, Hierarchical mushroom-like CoNi<sub>2</sub>S<sub>4</sub> arrays as a novel electrode material for supercapacitors. *Nano Energy* **3**, 36–45 (2014)
39. X.F. Lu, D.J. Wu, R.Z. Li, Q. Li, S.H. Ye, Y.X. Tong, G.R. Li, Hierarchical NiCo<sub>2</sub>O<sub>4</sub> nanosheets@hollow microrod arrays for high-performance asymmetric supercapacitors. *J. Mater. Chem. A* **2**(13), 4706 (2014)

**Publisher's Note** Springer Nature remains neutral with regard to jurisdictional claims in published maps and institutional affiliations.